Eur. J. Mineral.
2006, **18**, 449-462

The thermoelastic properties of $MgSO_4 \cdot 7D_2O$ (epsomite) from powder neutron diffraction and *ab initio* calculation

ANDREW D. FORTES[1]*, IAN G. WOOD[1], MARIA ALFREDSSON[1], LIDUNKA VOČADLO[1] and KEVIN S. KNIGHT[2,3]

[1]Research School of Geological and Geophysical Sciences, University College London, Gower Street, London, WC1E 6BT, United Kingdom
[2]ISIS Facility, Rutherford Appleton Laboratory, Chilton, Didcot, Oxfordshire, OX11 0QX, United Kingdom
[3]Natural History Museum, Cromwell Road, London, SW7 5BD, United Kingdom

Abstract: time-of-flight powder neutron diffraction has been used to measure the molar volume of $MgSO_4.7D_2O$ (i) from 1.8 – 300 K at ambient pressure, (ii) from 50 – 290 K at 1.4, 3.0, and 4.5 kbar, (iii) from 0 – 5.5 kbar at 290 K, and (iv) from 0 – 4.5 kbar at 50 K. The data have allowed us to determine the temperature dependence of the incompressibility, $(\partial K/\partial T)_P$, (thermodynamically equivalent to the pressure dependence of the thermal expansion, $(\partial\alpha/\partial P)_T$) of epsomite throughout its stability field. We observed that the *a*-axis exhibits negative thermal expansion, α_a, from 30 – 250 K at room pressure, turning positive above 250 K and being zero below 30 K. However, each of the crystallographic axes exhibits a sharp change in $(\partial\alpha/\partial T)$ at ~125 K, and this appears to correspond to significant changes in the axial incompressibilities with the *a*- and *c*-axes softening, and the *b*-axis stiffening considerably below ~125 K.

Our thermoelastic results are in agreement with *ab initio* calculations at zero Kelvin; however the calculations offer no obvious insight into the mechanism responsible for the change in behaviour at low temperature.

Key-words: epsomite, neutron diffraction, high-pressure, incompressibility, thermal expansion.

1. Introduction

Epsomite, $MgSO_4.7H_2O$, is a widespread evaporite mineral on Earth (see Hardie, 1984), being the stable phase in contact with a saturated solution at temperatures from 275 – 320 K (Fig. 1); it may also be abundant in the Martian regolith (*e.g.*, Feldman *et al.*, 2004: Zolotov *et al.*, 2004). In addition, epsomite is known to occur as an aqueous alteration product in chondritic meteorites (Frederiksson & Kerridge, 1988) and is therefore thought likely to be present in many rocky asteroids. The presence of salts such as $MgSO_4$, Na_2SO_4, and Na_2CO_3 in chondritic meteorites led to the suggestion that the water-rich icy moons of the Gas Giant planets would have ice mantles dominated by multiply-hydrated salts, including epsomite, resulting from leaching by aqueous fluids during accretion and differentiation (Kargel, 1991), with implications for the geophysics and astrobiology of these objects (Hogenboom *et al.*, 1995; Kargel *et al.*, 2000; Spaun & Head, 2001; McKinnon, 2002; McKinnon & Zolensky, 2003). This suggestion has been supported by observational evidence from the Near Infrared Mapping Spectrometer (NIMS) instrument aboard the Galileo spacecraft, which orbited Jupiter from 1995 to 2003. NIMS collected multispectral images of the surfaces of Jupiter's icy moons, Europa, Ganymede, and Callisto and these spectra have been interpreted as showing deposits of hydrated alkali salts (McCord *et al.*, 2001; Dalton *et al.*, 2005; Orlando *et al.*, 2005).

If we are to incorporate epsomite as a major rock-forming mineral in geophysical models of icy-moon interiors we must know its bulk physical properties under conditions far removed from room pressure and temperature; the icy Galilean moons have surface temperatures of ~ 90 K and core-mantle pressures may be ~ 1.5 GPa.

We therefore review briefly the literature relating to epsomite at high pressure and low temperature; an extensive review of earlier literature is presented elsewhere (Fortes, 2005).

The structure of epsomite was solved by Baur (1964) and subsequently studied by Ferraris *et al.* (1973), using neutrons, and Calleri *et al.* (1984) using X-rays. The space group is $P2_12_12_1$ with $Z = 4$ and cell parameters $a = 11.866$ Å, $b = 11.998$ Å, $c = 6.855$ Å at 295 K. The structure (Fig. 2) consists of SO_4^{2-} tetrahedra and $Mg(H_2O)_6^{2+}$ octahedra linked together by ordered hydrogen bonds. The seventh water molecule is not coordinated to the magnesium, but occupies a 'void' in the structure.

The earliest high-pressure work was carried out by Bridgman (1948a,b) upon polycrystalline and single

*E-mail: andrew.fortes@ucl.ac.uk

DOI: 10.1127/0935-1221/2006/0018-0449

0935-1221/06/0018-0449 $ 6.30

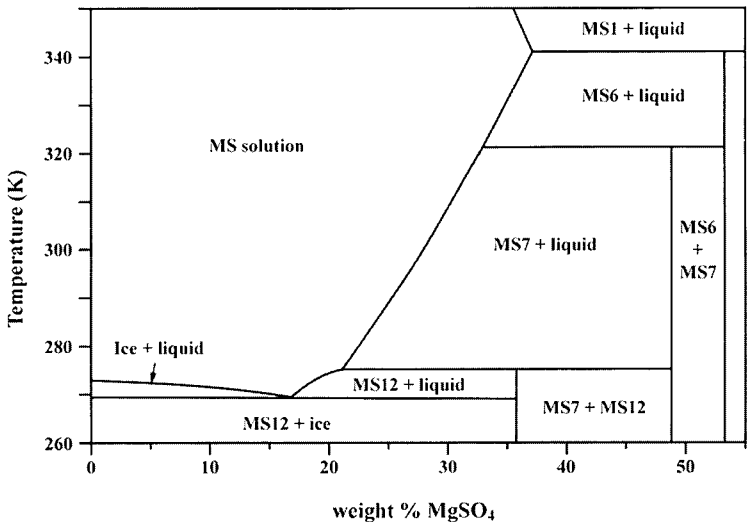

Fig. 1. Temperature – composition phase diagram for the binary system H_2O – $MgSO_4$ at atmospheric pressure showing the solid phases in equilibrium with aqueous solutions of magnesium sulfate ('MS solution'). The marked phases are, H_2O ice Ih, MS12 = $MgSO_4.12H_2O$ (Fritzsche's salt); MS7 = $MgSO_4.7H_2O$ (epsomite); MS6 = $MgSO_4.6H_2O$ (hexahydrite); MS1 = $MgSO_4.H_2O$ (kieserite).

crystal epsomite at pressures up to 4 GPa in a piston-cylinder apparatus. Bridgman observed a sluggish phase transition between 1.0 – 1.5 GPa, and suggested two further sluggish transitions at ~ 2.5 GPa.

The piston compression method was subsequently employed by Livshits *et al.* (1963) in work on crystalline hydrates of magnesium sulfate. These authors claimed to have observed the following series of phase transitions; I ↔ II (~ 0.45 GPa); II ↔ III (~ 1.2 GPa); III ↔ IV (~ 1.6 GPa); and IV ↔ V (~ 2.5 GPa). Of these, the II ↔ III transition may correspond to Bridgmans' first phase change, and the IV ↔ V transition to one of Bridgmans' 2.5 GPa phase changes. Livshits *et al.* (1963) also reported weak evidence for breaks in their pressure–volume curves at ~ 0.2 GPa and at 0.7 – 0.8 GPa.

More recently, a number of groups have studied melting relations in the H_2O - $MgSO_4$ system (Hogenboom *et al.*, 1995, to 0.4 GPa; Grasset *et al.*, 2001a,b, to ~ 2 GPa; Nakamura, 2003, to ~ 5 GPa) and in more complex ternary systems considered applicable to Europa's subsurface ocean and icy crust; *e.g.*, H_2O - $MgSO_4$ - H_2SO_4 (Hogenboom *et al.*, 2001). Of these studies, Grasset *et al.* (2001a,b) noted, by visual observation, a probable phase transition in epsomite at 0.6 GPa.

The only measurements at low temperature relate to the heat capacity. The isobaric heat capacity, C_P, of epsomite was measured from 15 – 300 K (Cox *et al.*, 1955) in order to correct the measured heat capacity of hexahydrite ($MgSO_4.6H_2O$). However, the C_P values for the heptahydrate were not published and, to our knowledge, are lost. Hence, there only remains the measured value of C_P for the heptahydrate in the range 311 – 321 K (Kopp, 1865, p156) and four values, determined by Differential Scanning Calorimetry, at 223, 263, 273, and 298 K (Prieto & Kargel, 2001).

Clearly, there is not complete agreement between the preceding high-pressure experiments, and considerable doubt remains as to the polymorphic phase behaviour of epsomite under pressure. Essentially nothing is known about the structure and behaviour of epsomite at low temperatures.

Our goals in this work are therefore as follows;

To establish the structure of epsomite at low temperature (*i.e.*, close to absolute zero).

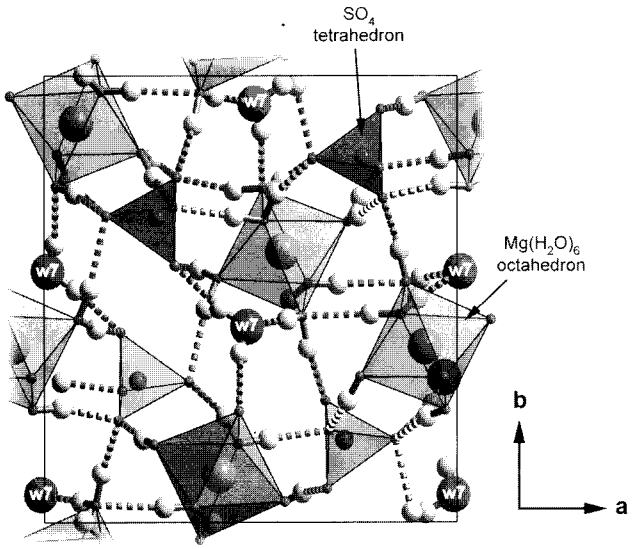

Fig. 2. Polyhedral representation of the epsomite crystal structure viewed along the *c*-axis.

To determine the coefficient of volume thermal expansion, α_V, throughout the stability field of the low-pressure phase.

To measure the incompressibility, K_0, and its temperature dependence, $\partial K/\partial T$, for epsomite.

To constrain the pressure stability field of the ambient-pressure phase of epsomite.

The principal method of choice for achieving most of these goals is neutron diffraction. Neutrons are necessary to determine the location of hydrogen atoms in the crystal structure, although in practice deuterated analogues must be used to avoid the large incoherent scattering of hydrogen, which contributes to the background of the diffraction pattern (*e.g.*, Finney, 1995). It is worth observing that the only neutron diffraction experiment to date (Ferraris *et al.*, 1973) was done with *hydrogenous* epsomite. This is the first time that a neutron scattering experiment has been carried out using a deuterated sample.

We have therefore carried out three experimental runs on the High Resolution Powder Diffractometer (HRPD) (Ibberson *et al.*, 1992) at the ISIS facility, Rutherford Appleton Laboratory, U.K. HRPD is ideally suited to rapid and accurate determination of cell parameters by virtue of its essentially constant resolution ($\Delta d/d$ = 10^{-4} in the backscattering detectors) across all d-spacings. Moreover, the instrument is sensitive to shifts in peak positions roughly two orders of magnitude smaller than the nominally stated resolution.

The first experiment was carried out at atmospheric pressure with the aim of satisfying goals 1) and the first part of 2). The second and third experiments were carried out in pressure vessels, and allowed us to address goals 2), 3), and 4).

In addition to experiments, we have calculated the structural and elastic properties of epsomite from first principles using density functional theory (DFT). Computational simulation of epsomite has a number of benefits. We can calculate the properties of fully hydrated 'ideal' heptahydrate crystals, wholly uncontaminated by defects, fluid inclusions, *etc.* DFT calculations allow us to determine the density and elasticity of epsomite in the athermal limit (*i.e.*, at zero Kelvin without zero point vibrational energy), typically to within a few percent. The computational study was made to help resolve outstanding questions relating to the elasticity of epsomite where there is considerable disagreement in the published elastic constants (see Section 4). Furthermore, we can study the ambient-pressure phase of epsomite at pressures far outside its stability field; we have made calculations over a pressure range approximately ten times larger than the known natural stability field of epsomite. Access to this wider phase space means we can more accurately define subtleties in the shape of the P-V curve which are described by, for example, the pressure derivative of the incompressibility, K'_0. We can also characterise small structural changes, such as the pressure strengthening of hydrogen bonds or changes in the shape of the unit cell, which may be too small to be observed experimentally.

We begin by describing the computational and experimental methods in Section 2; we then present the results in Section 3, and discuss our interpretation of the results in Section 4.

2. Method

2.1 Computational method

The plane-wave pseudopotential method, based on density functional theory (Hohenberg & Kohn, 1964: Kohn & Sham, 1965), was used for calculating the total energy of the crystal lattice.The Perdew-Wang generalised gradient corrected functional (PW91, Perdew, 1991; Perdew & Wang, 1992) was applied to represent the exchange-correlation potential, this form of the generalised gradient approximation (GGA) having been demonstrated to yield the most accurate results in hydrogen-bonded systems (Tsuzuki & Lüthi, 2001; Langlet *et al.*, 2004) despite not correctly representing dispersion forces. Core electrons are replaced by ultrasoft non-normconserving pseudopotentials (Vanderbilt, 1990), themselves formulated within the GGA. Total energy calculations were performed using the VASP (Vienna *Ab initio* Simulation Package) code (Kresse & Furthmüller, 1996). Convergence tests were carried out to optimise the $\vec{k}$-point sampling of the Brillouin zone within the Monkhorst-Pack scheme (Monkhorst & Pack, 1976), and the kinetic energy cut-off of the plane-wave basis set. It was found that a 4×4×4 grid with 8 symmetrically unique $\vec{k}$-points in the irreducible wedge, combined with a kinetic energy cut-off of 1100 eV, yielded total energy convergence to better than 10^{-4} eV per atom (~ 10^{-2} eV per unit cell). A series of fixed volume calculations were then performed in which the ions were allowed to move according to the calculated Hellman-Feynman forces and the cell shape was allowed to vary. For each volume specified the structure was relaxed via the conjugate-gradient technique in order to optimise the lattice parameters and internal coordinates.

2.2 Experimental method (Time-of-flight powder neutron diffraction)

Crystals of deuterated epsomite were grown from supersaturated solutions of $MgSO_4$ (Sigma-Aldrich > 99.5 % purity) in D_2O (Aldrich Chemical Co. > 99 atom % D) in a sealed pyrex flask. In the first instance these were air dried and visually compared with the known habit of epsomite. Crystals were then triturated and X-ray powder diffraction patterns collected to confirm that the material was epsomite. For the neutron diffraction experiments, wet crystals of deuterated epsomite were separated from the mother liquor in a glove bag and dried under helium gas for about an hour; drying for longer periods resulted in the formation of significant quantities of hexahydrite ($MgSO_4.6H_2O$). The dry crystals were ground and sieved to a maximum grain size of 425 μm. This powder was used for the ambient pressure experiment. The remaining dry powder was ground to a finer consistency and sieved to a maximum grain size of 100 μm. This finer powder was used for the high-pressure room-temperature experiment. A

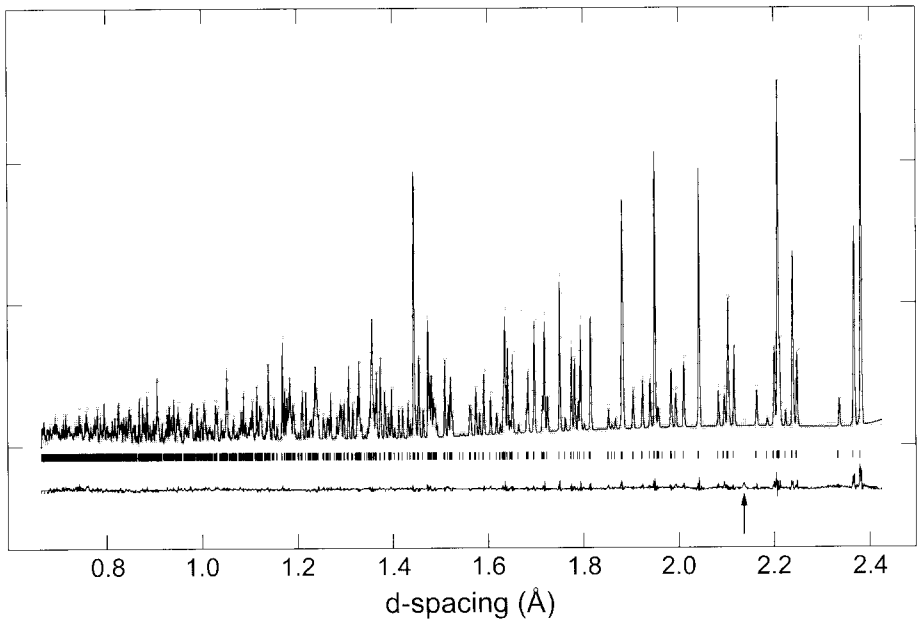

Fig. 3. Diffraction pattern of epsomite at 2 K. 14 hour integration in the HRPD backscattering banks ($2\theta = 168°$).

second aliquot was dried, ground, and sieved to a maximum grain size of 150 μm for use in the high-pressure low-temperature experiment.

2.2.1 The ambient pressure experiment.

For the ambient pressure experiment, the < 425 μm fraction of powdered $MgSO_4.7D_2O$ was loaded – in the open air – into an aluminium-framed sample container (internal volume 6.2 cm^3) with vanadium windows. This 'slab-can' was attached to a cryostat centre stick and loaded into a pre-cooled Orange cryostat. The cryostat was positioned in the neutron beam and the sample temperature was reduced to 1.8 K. Diffraction data were collected in the backscattering and 90° detectors of HRPD (Fig. 3 and 4) at 1.8 K for ~ 14 hours to allow for a structure refinement using the GSAS package (Larsen & von Dreele 1988). Diffraction patterns were then collected on warming to 5 K, and at 5K intervals thereafter (counting for ~ 25 minutes with 3 additional minutes of thermal equilibration at each temperature point) up to 300 K. At 300 K, diffraction data were

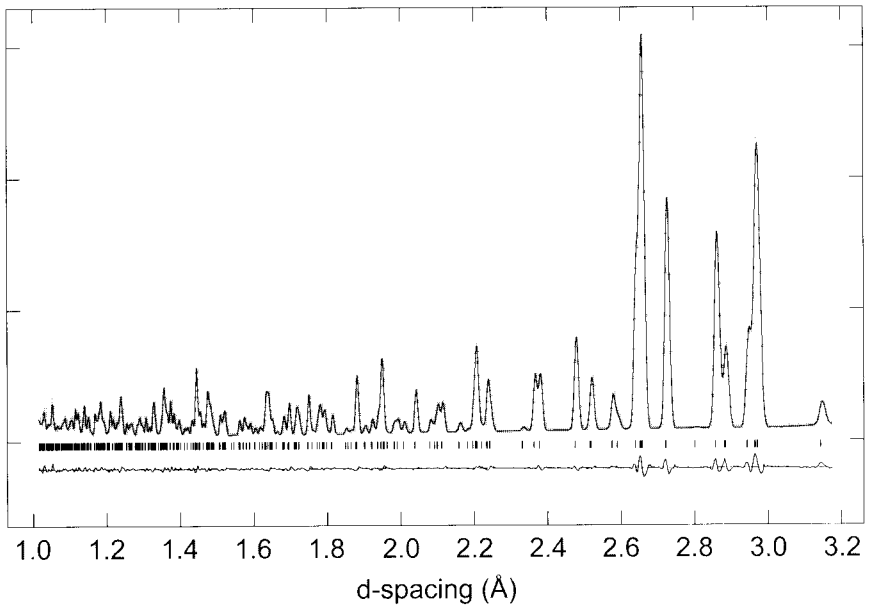

Fig. 4. Diffraction pattern of epsomite at 2 K. 14 hour integration in the HRPD 90° detector bank.

collected for ~ 4 hours. These patterns were suitable for refinement of unit cell parameters* with a precision of better than 1 part in 70,000.

*Note that cell dimensions were extracted from all of the diffraction patterns except for the 2 K room-pressure point, using the CAILS (cell and intensity least squares) refinement routine in CCSL (Brown and Matthewman 1993, after Pawley 1981).

2.2.2 The high-pressure room-temperature experiment.

Roughly 1 cm^3 of the 100 μm fraction of powdered $MgSO_4.7D_2O$ was loaded into a TiZr pressure vessel, which allows for continuous hydrostatic loading of the sample under (in this instance) argon gas up to ~ 0.55 GPa. The TiZr can was attached to a cryostat centre stick and sealed under a nominal pressure of ~ 100 bar before being loaded into an Orange cryostat and placed in the beam line.

Diffraction patterns were then collected with the 90° detectors of HRPD at 0.1, 1.1, 2.2, 3.3, 4.4, and 5.5 kbar (at 290.3 ± 0.3 K) upon compression, and at 5.0, 3.9, 2.8, 1.7, and 0.6 kbar upon decompression, counting for ~ 90 minutes at each pressure point. These patterns were suitable for refinement of unit cell parameters with a precision of ~ 1 part in 10,000 for the *a*- and *c*-axes, and ~ 1 part in 30,000 on the *b*-axis.

2.2.3 The high-pressure low-temperature experiment.

Roughly 1 cm^3 of the 150 μm fraction of powdered $MgSO_4.7D_2O$ was loaded into an aluminium pressure vessel, which allows for continuous hydrostatic loading of the sample under (in this second instance) helium gas up to ~ 0.45 GPa. The Al can was attached to a cryostat centre stick and sealed under a nominal pressure of ~ 75 bar before being loaded into an Orange cryostat and placed in the beam line.

Diffraction patterns were then collected with the 90° detectors of HRPD at 10 K intervals (between 50 – 290 K) whilst; (i) cooling along the 1.4 kbar isobar, (ii) warming along the 3.0 kbar isobar, (iii) and cooling along the 4.5 kbar isobar. From 4.5 kbar, the sample was then decompressed along the 50 K isotherm, with diffraction patterns being collected at roughly half kilobar intervals.

By virtue of the thinner walls of the aluminium can, it was possible to refine unit cell parameters with a precision comparable to the high-pressure room-temperature experiment after just 30 minutes of data collection at each P,T point. The diffraction patterns of epsomite under both helium and argon gas are the same indicating that helium molecules are not penetrating the structure, as they do in water ice for example (*e.g.*, Fortes *et al.*, 2005).

3. Results

3.1 Computational results

Structural relaxations were carried out at a series of fixed unit cell volumes from ~ 840 $Å^3$ to ~ 1135 $Å^3$ (covering the pressure range from –2.14 to +6.13 GPa) at which the total energy of the crystal was calculated. An integrated form of the third-order Birch-Murnaghan equation of state (BMEOS: Birch, 1952) was fitted to the E(V) points to determine the zero-pressure density, ρ_0, the zero-pressure bulk modulus, K_0, and its first pressure derivative, $(\partial K / \partial P)_0$ or K'_0 (Fig. 5). The lattice parameters as a function of the BMEOS3-derived pressure were fitted with polynomials, and these were differentiated to find the axial incompressibility along each of the three unit cell axes; *i.e.*, $K_a = (1 / a)(\partial a / \partial P)$, and $K'_a = (\partial K_a / \partial P)_T$. The parameters resulting from these various fits are given in Table 2, and a discussion of how they compare with experimental values follows in Section 5.

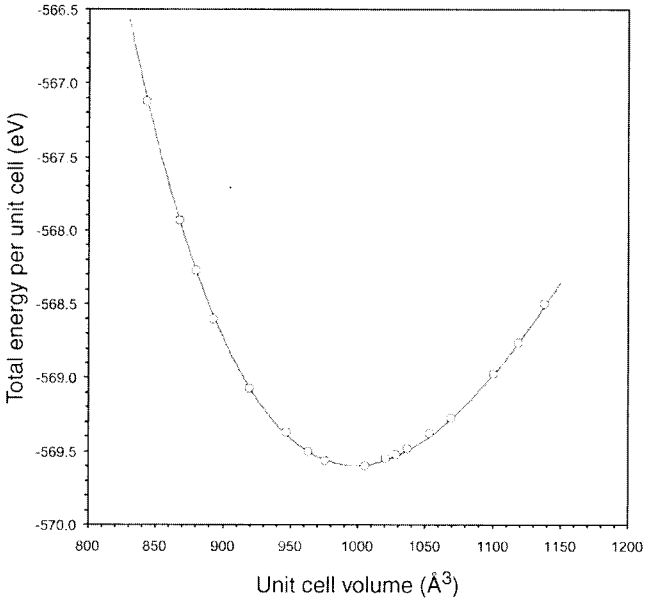

Fig. 5. The calculated E(V) curve of epsomite. The solid line is a 3rd order Birch-Murnaghan equation of state, the parameters of which are given in Table 2.

The *b*-axis is clearly much softer than the other two axes. The net result of this is that the *b/a* ratio changes as a function of pressure, shrinking until the unit cell becomes metrically tetragonal at a calculated pressure of 0.74 GPa. The *b/a* ratio continues to decrease with pressure; in other words, the *a*-axis become the long axis, and the *b*-axis, the intermediate-length axis.

3.2 Experimental results

3.2.1 The structure of epsomite at 2 Kelvin

At 2 K, data were collected in the time-of-flight (tof) window from 32 – 120 milliseconds using the backscattering (2θ = 168°, d-spacing range of 0.67 – 2.49 Å) and 90° detector banks (d-spacing range of 0.93 – 3.50 Å) on HRPD (Fig. 3 and 4). Neutrons were counted for ~ 14 hours (480 μA). The sample was subsequently weighed so that an appropriate absorption correction could be applied

Table 1. The refined structural parameters for epsomite at room pressure, 2K.

Unit cell	Powder statistics		fitted		minus background	
a = 11.89713(4) Å	Histogram	Data	R_{wp}	R_p	R_{wp}	R_p
b = 11.90851(4) Å	1	4322	2.99 %	2.61 %	3.19 %	2.96 %
c = 6.78729(3) Å	2	1631	2.56 %	1.95 %	2.51 %	2.07 %
V = 961.603(6) Å^3	Total	5953	2.70 %	2.29 %	2.69 %	2.45 %
Fractional atomic coordinates						
Atom	x		y	z	U_{iso} (x100) Å^2	
Mg	0.41931(33)		0.10562(32)	0.0393(8)	0.53(9)	
S	0.72310(51)		0.18174(49)	0.4978(12)	0.17(16)	
sO1	0.67859(28)		0.07070(25)	0.4310(6)	0.24(8)	
sO2	0.84651(28)		0.17922(27)	0.4782(6)	0.50(9)	
sO3	0.68582(28)		0.20434(24)	0.6975(6)	0.15(8)	
sO4	0.67809(32)		0.27187(27)	0.3646(6)	0.45(9)	
wO1	0.26201(33)		0.17315(34)	0.0004(8)	1.15(10)	
wO2	0.46935(35)		0.24881(27)	0.1961(7)	0.42(9)	
wO3	0.46353(39)		0.17443(29)	0.7749(7)	0.51(9)	
wO4	0.57480(32)		0.04448(28)	0.0754(7)	0.94(9)	
wO5	0.37148(32)		0.95860(31)	0.8890(8)	0.69(10)	
wO6	0.35937(40)		0.03815(27)	0.2939(8)	0.76(9)	
wO7*	0.49961(29)		0.43503(31)	0.9345(6)	0.20(8)	
D11	0.23099(31)		0.22029(32)	0.1028(7)	1.86(10)	
D12	0.23445(33)		0.19687(30)	0.8746(7)	1.92(10)	
D21	0.42040(35)		0.27324(27)	0.3051(6)	1.92(10)	
D22	0.54585(37)		0.25374(27)	0.2558(7)	1.92(10)	
D31	0.42060(33)		0.22382(34)	0.6911(7)	1.77(10)	
D32	0.54590(34)		0.18209(30)	0.7427(6)	1.59(9)	
D41	0.62292(32)		0.05379(26)	0.1949(6)	1.65(10)	
D42	0.60617(28)		0.97523(29)	0.0189(7)	1.83(9)	
D51	0.36205(27)		0.89144(31)	0.9724(7)	2.13(10)	
D52	0.42026(32)		0.94056(29)	0.7764(7)	1.95(10)	
D61	0.28203(35)		0.02765(30)	0.3289(6)	2.05(10)	
D62	0.40230(34)		0.99809(34)	0.3972(6)	2.05(10)	
D71*	0.43179(29)		0.48285(30)	0.9538(6)	2.38(10)	
D72*	0.47695(30)		0.36651(31)	0.0038(7)	1.97(9)	

The Rietveld powder statistics are defined as, $R_P = \sum|I_o - I_c|/\sum I_o$(where I_o and I_c are observed and calculated intensities, respectively), and $R_{wp} = \sqrt{M_p/\sum wI_0^2}$ (where M_p is the Rietveld minimization function $Mp = \sum w(I_o - I_c)^2$, and wI_0^2 the weighted square of the observed intensities). The reduced $\chi^2 = M_p/N_{obs} - N_{var}$. Asterisks indicate the seventh 'uncoordinated' water molecule.

to the data. The structure was refined using the general structure analysis system (GSAS) code developed by Larson & von Dreele (1988) starting from the neutron-derived structure of Ferraris *et al.* (1973). At the start of the refinement, isotropic temperature factors (U_{iso}) for the four sulfate oxygens, for the six Mg-coordinated water oxygens, for the twelve deuterons attached thereto, and for the two deuterons bound to the seventh water oxygen, were constrained to be equal. Peak profile shapes were modelled using GSAS function 3, and corrections were included for extinction effects and sample texture (using a 12th order spherical harmonic model). In the final least squares cycles, individual temperature factors were allowed to

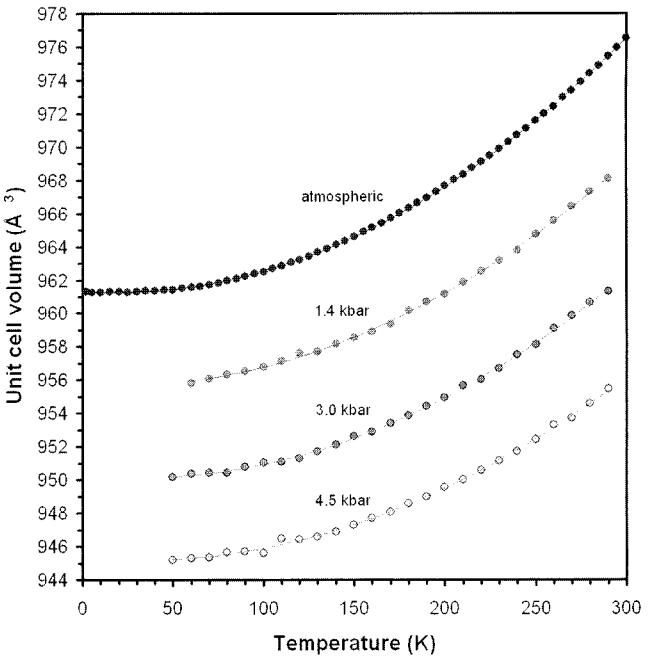

Fig. 6. Temperature dependence of the unit cell volume of deuterated epsomite at 0.001, 1.4, 3.0, and 4.5 kbar.

freely refine. The final refinement, over 5953 data points yielded R_{wp} = 2.70 %, R_p = 2.29 %, and reduced χ^2 = 19.89 for 166 variables (see Table 1 for a breakdown and definitions of the powder statistics).

There is some precedent for sulfate hydrates to form lower symmetry structures at reduced temperatures; sodium ammonium sulfate dihydrate, for example, undergoes a ferroelectric phase transition from $P2_12_12_1$ to $P2_1$ on cooling below 111 K (Lipiński *et al.*, 2001). Given the changes in physical properties at low temperature reported in the following sections, we allowed that such a transformation might have occurred in epsomite. We therefore used CAILS to perform a structurally unbiased test of this hypothesis: in the orthorhombic setting, the unit cell was found to be a = 11.89581(3) Å, b = 11.90750(3) Å, c = 6.78649(2) Å (R_{wp} = 2.78 %, R_p = 2.23 %, χ^2 = 8.623 for 141 variables and 1567 observations), whereas in the monoclinic setting the unit cell dimensions are a = 11.89601(5) Å, b = 11.90736(6) Å, c = 6.78632(4) Å, β = 89.9653(7)° (R_{wp} = 2.49 %, R_p = 1.95 %, χ^2 = 7.202 for 195 variables and 1567 observations). The statistical improvement is marginal, but the angle β is significantly different from 90° by 0.0347(7)°. Hence, we cannot rule out a very slight monoclinic distortion at low temperatures.

3.2.2 Thermal expansion of $MgSO_4.7D_2O$

3.2.2.1 Volume thermal expansion

The HRPD ambient-pressure data set consists of 61 data points at 5 K intervals from 2 – 300 K (Fig. 6). These data are fit extremely well (R^2 = 99.9952 %) by a simple

second order polynomial, $aT^2 + bT + V_0$, with a = 1.906(6) $\times 10^{-4}$ Å^3 K^{-2}, b = -6.49(20) $\times 10^{-3}$ Å^3 K^{-1}, and V_0 = 961.296(14) Å^3. The maximum difference between the data and the fitted curve is just 0.0071 %. The coefficient of volume thermal expansion, $\alpha_V = (1/V)(\partial V/\partial T)_P$, found by numerical differentiation of the unit cell volume data, and by differentiation of the second order fit to V, is shown in Fig 7. The narrow region of negative volume thermal expansion below ~15 K is probably an artefact of the polynomial fit, but the remarkable linearity of the remainder of the plot is real. It is obvious that α_V shows no indication of 'turning over' at temperatures close to the dehydration transition (320 K).

At higher pressures (Fig. 6), second order polynomials also provide good fits to the data (three sets of 24 points). At 1.4 kbar, a = 1.705(47) $\times 10^{-4}$ Å^3 K^{-2}, b = –6.7(17)x10^{-3} Å^3 K^{-1}, V_0 = 955.73(13) Å^3 (R^2 = 99.93 %); at 3.0 kbar, a = 1.704(41) $\times 10^{-4}$ Å^3 K^{-2}, b = –11.1(14) $\times 10^{-3}$ Å^3 K^{-1}, V_0 = 950.32(11) Å^3 (R^2 = 99.93 %); at 4.5 kbar, a = 1.537(50) $\times 10^{-4}$ Å^3 K^{-2}, b = –10.0(17) $\times 10^{-3}$ Å^3 K^{-1}, V_0 = 945.34(13) Å^3 (R^2 = 99.87 %). Note that these fits should not be extrapolated below 50 K or above 290 K; neither are they strictly isobaric since the pressure drifted by order 100 bar during warming and cooling runs even with a buffer volume in the pressure line.

For comparison with earlier results on hydrogen-bonded crystals (*e.g.*, Fortes *et al.*, 2003, 2005) the ambient-pressure data points were also fitted with a second-order approximation to the Grüneisen zero-pressure equation of state (*e.g.*, Wallace 1998), in which the thermal expansion is considered equivalent to elastic strain such that,

$$V(T) = V_{0,0}\left[1 + \frac{E(T)}{Q - bE(T)}\right] \quad (1)$$

where $V_{0,0}$ is the unit cell volume at zero pressure and temperature, $b = {}^1/_2 (K'_{0,0} - 1)$ and $Q = (V_{0,0} K_{0,0} / \gamma)$. $K_{0,0}$ is the zero pressure and temperature isothermal bulk modulus, $K'_{0,0}$ is its first derivative with respect to pressure, and γ is the thermal Grüneisen parameter. The internal energy due to lattice vibrations, E(T), is determined *via* a Debye model (*e.g.*, Ashcroft & Mermin 1976):

$$E(T) = \frac{9nk_BT}{(\theta_D/T)^3}\int_0^{\theta_D/T}\frac{x^3}{e^x - 1}dx \quad (2)$$

where θ_D is the Debye temperature, n is the number of atoms per unit cell, and k_B is the Boltzmann constant; the integral term is evaluated numerically. This approach has been previously used with success on 'hard' materials such as FeSi (Vočadlo *et al.*, 2002) and $KMgF_3$ (Wood *et al.*, 2002).

When Eq. 1 is fitted to our V(T) data the fit is excellent, both in terms of unit cell volume and the thermal expansivity. However, the elastic parameters resulting from the fit are not sensible; $K_{0,0} / \gamma$ = 76.4 GPa and $K'_{0,0}$ = 56.7. As we have found with other hydrogen-bonded crystals, such as $ND_3.2D_2O$ (Fortes *et al.*, 2003) and D_2O ice II (Fortes *et al.*, 2005), the internal energy is better represented by two Debye moments with very different characteristic temperatures, θ_D^A and θ_D^B;

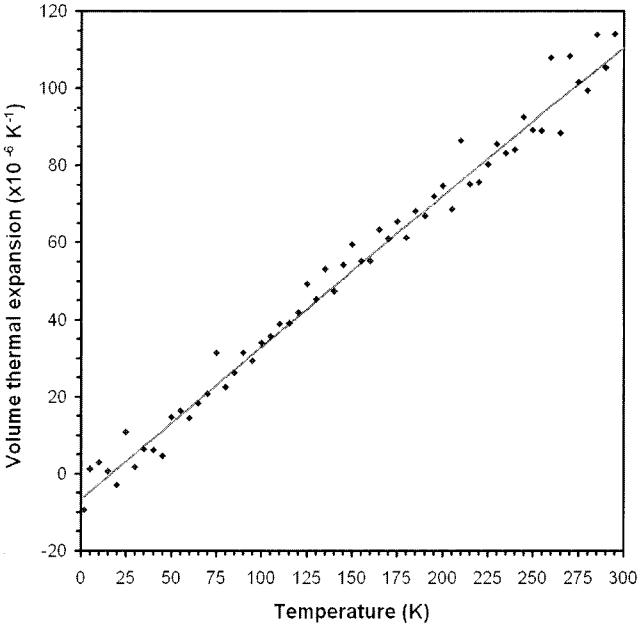

Fig. 7. Temperature dependence of the volume thermal expansion coefficient, α_V, for deuterated epsomite at ambient pressure. Points are from numerical differentiation of unit cell volume data; the solid line is from differentiation of a polynomial fit to the same data.

$$E = 9nk_B\left[Xf\left(\frac{\theta_D^A}{T}\right) + Yf\left(\frac{\theta_D^B}{T}\right)\right] \quad (3)$$

where $f(\theta_D / T)$ is the Debye function, n is the number of atoms per molecule, and X and Y are mixing parameters. In the absence of heat capacity measurements for epsomite, we have used as a proxy the measured heat capacity of the isostructural compound goslarite, $ZnSO_4.7H_2O$ (Barieau & Giauque, 1950), since its molar heat capacity near room temperature is similar to the few known values for epsomite (Kopp, 1865; Prieto & Kargel, 2001). The parameters resulting from the fitting of Eq. 3 to the heat capacity data for goslarite are; θ_D^A = 238 ± 5 K, θ_D^B = 1166 ± 6 K, X = 0.260 ± 0.007, and Y = 0.602 ± 0.013. These values are very similar to the other hydrogen-bonded crystals we have investigated; the Debye temperatures correspond to vibrational wavenumbers of ~ 165 cm^{-1} and 810 cm^{-1} and probably represent the translational and rotational excitations, ν_T and ν_R, of the water molecules in the structure, which likely dominate the heat capacity in the temperature range we are concerned with.

Equation 1 was refitted to the V(T) data using the double-Debye model, with E(T) fixed from fitting Eq. 3 to the heat capacity of goslarite rather than having θ_D as a free variable. The elastic parameters resulting from this fit are somewhat more sensible: $V_{0,0}$ = 961.15 ± 0.02 Å^3, ($K_{0,0} / \gamma$) = 31.9 ± 0.3 GPa, although $K'_{0,0}$ = 26 ± 1. This fit is nonetheless visibly poorer than the polynomial fit described above; the maximum difference between the data and the fitted curve is twice as large (0.016 %), being worse below ~ 150 K. However, this is a region in which there is considerable complexity in the axial expansivities

(see below), so we should not expect the Debye model to give results as good as those we have obtained for the more isotropic materials ammonia dihydrate and ice II.

3.2.2.2 Axial expansivities

The regularity of the volume expansion curves belies a considerable amount of complexity in the thermal expan-

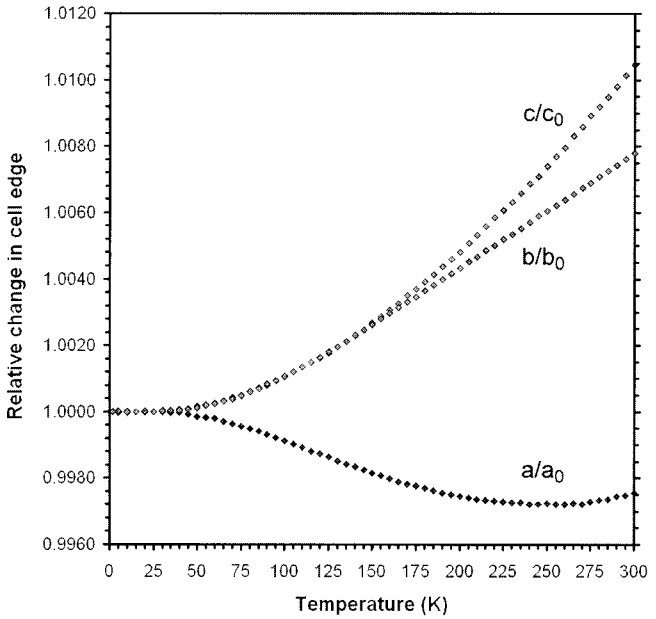

Fig. 8. Relative change in unit cell dimensions as a function of temperature, at room pressure, for deuterated epsomite.

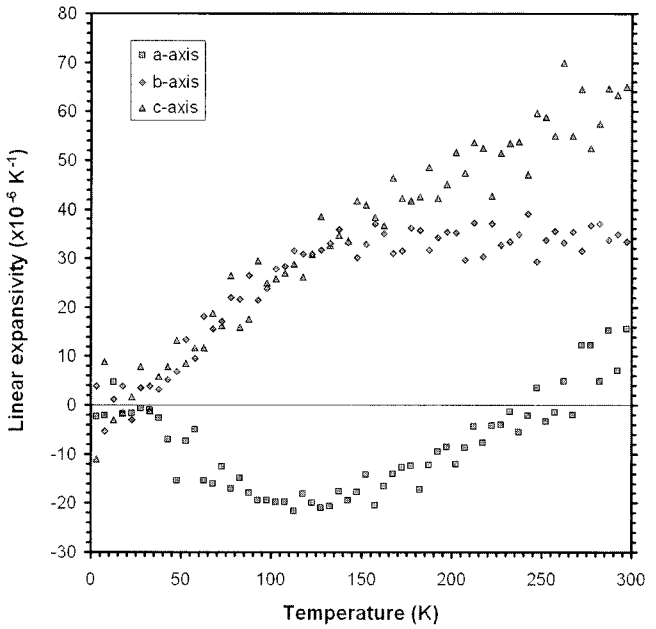

Fig. 9. Thermal expansivities of the three unit cell edges in deuterated epsomite at room pressure. Points are from numerical differentiation of unit cell edge lengths.

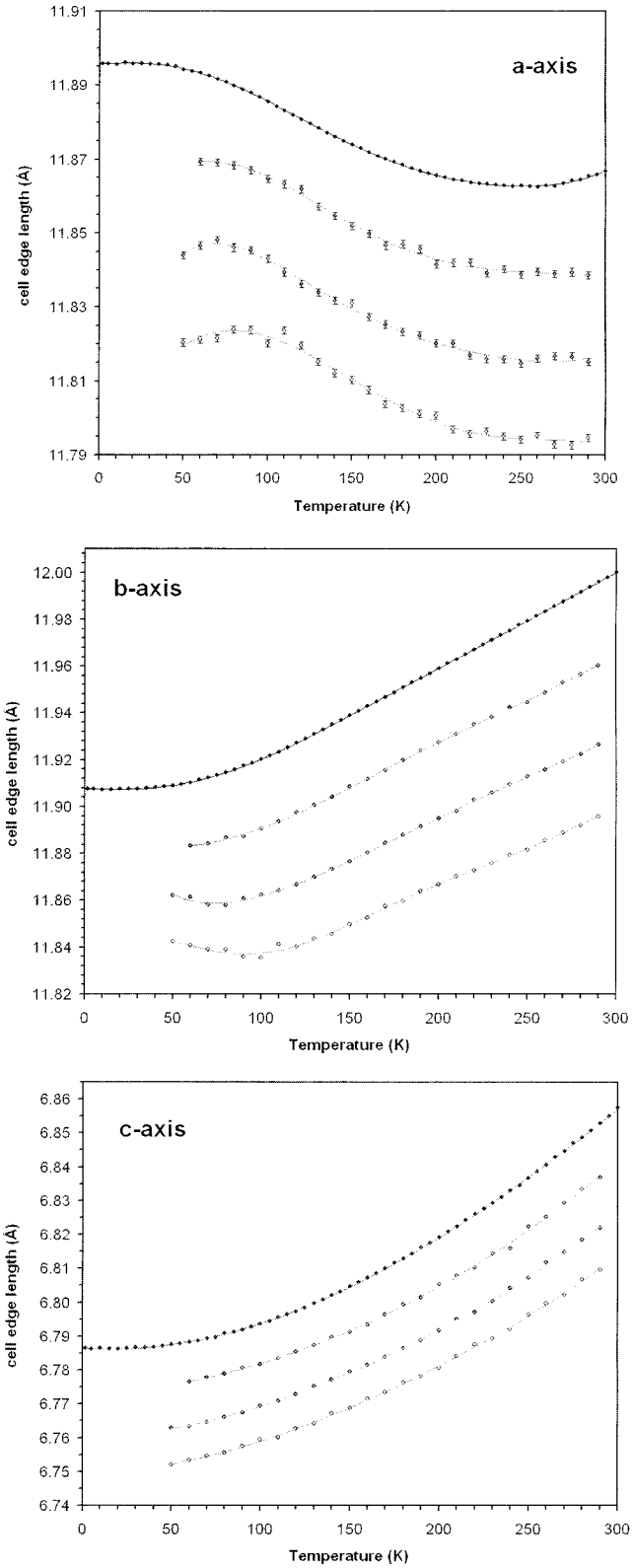

Fig. 10a-c.The temperature dependence of a) the *a*-axis, b) the *b*-axis, and c) the *c*-axis length at (from the top down) 0.001, 1.4, 3.0, and 4.5 kbar. Note that the 50 K datapoints at 1.4 kbar were lost due to a minor technical problem. At ambient pressure, the symbols are much bigger than the estimated standard errors; at higher pressure, for the *b*- and *c*-axes, the ESDs are similar to the size of the symbols used; ESDs for the *a*-axis are shown by error bars.

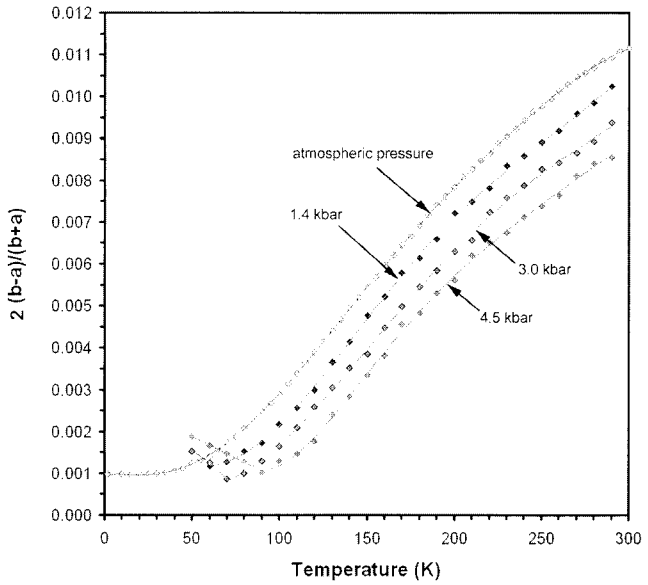

Fig. 11. The strain between the *a*- and *b*-axes as function of temperature at four pressures; lines are polynomials fitted to the data.

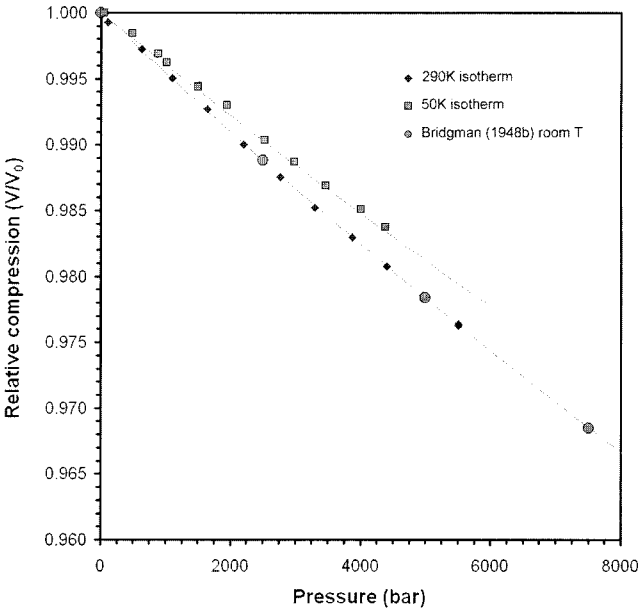

Fig. 12. Relative volume compression along the 290 K and 50 K isotherms compared with Bridgman's 1948 data. Solid lines are fitted equations of state; parameters in Table 1.

sion behaviour of the individual crystallographic axes. As Fig. 8 shows, the *a*-axis exhibits negative thermal expansion (NTE) from ~ 30 K up to 250 K, whereafter the expansivity gradually turns positive. In itself, this is not surprising; orthorhombic $NiSO_4.7H_2O$ exhibits NTE of its intermediate-length axis down to 25 K (Ptasiewicz-Bak *et al.*, 1997), and the *c*-axis of monoclinic $FeSO_4.7H_2O$ does not change in length significantly from 120 – 290 K (Fronczek *et al.*, 2001). Both of the other axes of epsomite exhibit more subtle changes in behaviour which only become obvious when $\partial\alpha/\partial T$ is plotted (Fig. 9). It seems that, far from being gradual, there is a sharp change in the thermal expansion near 125 K. At this temperature $\partial\alpha/\partial T$ for the *a*-axis changes sign, $\partial\alpha/\partial T$ for the *c*-axis drops slightly, and $\partial\alpha/\partial T$ for the *b*-axis becomes zero. Above 125 K, $\partial\alpha/\partial T$ for the *a*- and *c*-axes are roughly equal, $\sim 2 \times 10^{-7}$ K^{-2}.

The lower precision on the lattice parameters measured in the pressure cells limits the amount of information on the axial expansivities we can extract from the high-pressure data. However, we can see new phenomena at higher pressures, in addition to the same pattern of axial expansivities observed at room pressure (Fig. 10a-c). What is most interesting is the change in behaviour of the *a*- and *b*-axes below ~ 100 K at elevated pressures. The *a*-axis appears to assume a positive α at low temperature and high pressure, whereas the *b*-axis does the opposite. Purely from a qualitative point of view (that will be expanded upon quantitatively shortly) it is obvious from the divergence (*a*-axis) and convergence (*b*-axis) of the isobars in Fig. 10 that the linear incompressibility of the *a*-axis will drop (*i.e.*, it will become softer) below ~100 K, and that of the *b*-axis will rise suddenly. Some indication as to why this change occurs can be found by looking at the strain between the *a*- and *b*-axes. Figure 11 plots $2(b-a)/(b+a)$ against temperature for the four thermal expansion curves. Clearly, the strain bottoms out at a minimum value of 0.001 under all pressures investigated. At 3.0 and 4.5 kbar, the strain increases again on cooling below 70 K and 90 K respectively. The crystal appears to be 'avoiding' becoming metrically tetragonal, and this may be due to steric hindrance in the structure.

3.2.3 Incompressibility of $MgSO_4.7D_2O$

3.2.3.1 Bulk incompressibility

Diffraction patterns from epsomite were collected at 12 pressure points from 0.01 – 0.55 GPa along the 290 K isotherm (in the TiZr cell under Ar gas), and at 11 pressure points from 0.05 – 0.45 GPa along the 50 K isotherm (in the Al cell under He gas). These data were refined to obtain the cell parameters and subsequently the unit cell volume (Fig. 12). These data sets were each fitted with a third-order Birch-Murnaghan equation of state (BMEOS: Birch, 1952) to yield the following parameters. Along the 290 K isotherm; zero pressure unit cell volume, $V_{0,290}$ = 973.81(10) Å^3, zero pressure isothermal bulk modulus, $K_{0,290}$ = 21.5(4) GPa, and the first pressure derivative of the bulk modulus, $K'_{0,290}$= 5.5(14) (R^2 = 99.979 %). Along the 50 K isotherm; $V_{0,50}$ = 961.18(10) Å^3, $K_{0,50}$ = 24.9(8) GPa, and $K'_{0,50}$= 6(3) (R^2 = 99.937 %). Since K'_0 was very poorly determined, these data were subsequently refitted with $K'_{0,T}$ fixed at the value found from our *ab initio* calculations ($K'_0 \equiv 5.3$). The new fit parameters are given in Table 2; goodness of fit in each case only changed in the third decimal place of R^2. The fitted EoS is shown by the solid line in Fig. 12.

Considerably less precise bulk moduli can be determined at temperatures from 60 –280 K using isotherms in

Table 2. The bulk incompressibility and linear incompressibilities of epsomite.

		Speed of sound measurements			*Compression measurements*			*Ab initio*
		Sundara Rao (1950)[1]	Voronkov (1958)	Alexandrov *et al.* (1963)	Bridgman (1948b)[2]	This work (neutron)[3]	This work (neutron)[4]	This work (*ab initio*)[5]
K_0	(GPa)	43.5	28.99	22.2(7)	21.6	21.5(1)	25.0(2)	23.2(2)
K'_0		-	-	-	5.0	5.3	5.3	5.3(2)
K_a	(GPa)	190	112.4	74(4)	73.1	72(1)	66(2)	80.6(2)
K'_a		-	-	-	13.6	21	21	21.0(2)
K_b	(GPa)	86	94.6	56(5)	56.7	52.3(7)	76(2)	54.8(2)
K'_b		-	-	-	2.3	14(2)	14	13.9(2)
K_c	(GPa)	157	65.9	74(7)	64.5	73(1)	82(1)	77.6(2)
K'_c		-	-	-	51.4	20	20	20.1(2)

[1] This author gives no standard errors on the published elastic constants, and the values quoted here have an accuracy assumed similar to other experiments.
[2] 3rd order Birch-Murnaghan fits to Bridgman's tabulated, smoothed, results (0-10 kbar, room T)
[3] 3rd order Birch-Murnaghan fits to refined unit-cell volumes (0.1 – 5.5 kbar, T = 290 K) $V_{0,290}$ = 973.80(7) Å^3.K'_0 fixed at 5.3 (see text), K'_a fixed at 21, K'_c fixed at 20.
[4] 3rd order Birch-Murnaghan fits to refined unit-cell volumes (0.05 – 4.5 kbar, T = 50 K) $V_{0,50}$ = 961.17(7) Å^3. K'_0 fixed at 5.3 (see text), K'_a fixed at 21, K'_c fixed at 20.
[5] 3rd order Birch-Murnaghan fit to E(V) curve in the athermal limit. $V_{0,0}$ = 998.14(51) Å^3 and $E_{0,0}$ = -569.598(4) eV per unit cell.

Measured values, found by ultrasonic methods (columns 1- 3; see Table 4) and by hydrostatic compression (columns 4, 5, and 6) are compared with the values calculated from *ab initio* calculations (column 7). The derivation of these moduli is described further in the text.

the high-pressure thermal expansion data set (fixing $K'_0 \equiv 5.3$). Since each fit was to only three data points, the resulting bulk moduli are not very precise. The noise in the resulting incompressibilities can be suppressed by fitting the isothermal EoS to smoothed volume data; *i.e.*, by calculating V_{PT} from the second order polynomials reported in Section 3.1.1.

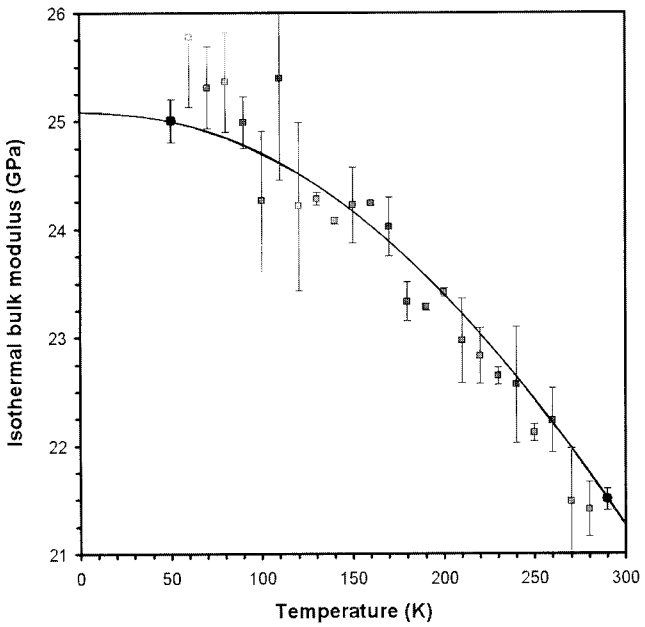

Fig. 13. Model temperature dependence of the isothermal bulk modulus (K_T). The two accurately determined isothermal bulk moduli, from the 50 K and 290 K data, are shown with bold symbols. The lighter toned symbols are fits to just three points at each temperature (see text).

We can now use these fits to model the temperature dependence of the incompressibility, K(T). Raju *et al.* (2002) derived an expression relating molar volume to bulk modulus which is simply an isobaric analogue of the Grover-Getting-Kennedy (GGK) relation (Grover *et al.*, 1973):

$$V(T) = V_0 + b \ln (K_{0,0} / K_{0,T}) \quad (4)$$

Figure 13 shows the best fit of this equation to the data, yielding b = 82(2) and $K_{0,0}$ = 25.23(5) GPa. The model bulk moduli, $K_{0,T}$, from 50 – 290 K are given in Table 3.

The slope of this model curve, $(\partial K/\partial T)_P$, is thermodynamically equivalent to the pressure dependence of the thermal expansion, $(\partial \alpha_V/\partial T)_T$. This is normally expressed through the isothermal Anderson-Grüneisen parameter, δ_T, where;

$$\delta_T = \frac{1}{\alpha_V K_T}\left(\frac{\partial K_T}{\partial T}\right)_P \quad (5)$$

The values of δ_T, given in Table 3, may then be used to derive the pressure dependence of the thermal expansivity *via*;

$$\left(\frac{\alpha}{\alpha_0}\right) = \left(\frac{V}{V_0}\right)^{\delta_I} \quad (6)$$

3.2.3.2 Axial incompressibilities

The same procedure as in Section 3.2.1. was used to fit each of the three unit cell edges, giving at 290 K; a_0 = 11.859(1) Å, K_a = 78(4) GPa, K'_a = 0(13) (R^2 = 99.86 %); b_0 = 11.9888(3) Å, K_b = 52.3(7) GPa, K'_b = 14(2) (R^2 = 99.99 %); c_0 = 6.8492(5) Å, K_c = 67(3) GPa, K'_c = 44(14) (R^2 = 99.92 %). Clearly, the pressure derivatives of the incompressibility for the *a*- and *c*-axes are very poorly determined from the data. Fixing these derivatives equal to the values found in *ab initio* calculations ($K'_a \equiv 21$ and K'_c

≡ 20) gives a_0 = 11.861(1) Å, K_a = 72(1) GPa (R^2 = 99.83 %), and c_0 = 6.8486(4) Å, K_c = 73(1) GPa (R^2 = 99.87 %). At 50 K, the pressure derivatives of the incompressibility were also fixed at their *ab initio* values ($K'_a \equiv 21$, $K'_b \equiv 14$, and $K'_c \equiv 20$) to give a_0 = 11.895(1) Å, K_a = 66(1) GPa (R^2 = 99.43 %), b_0 = 11.907(1) Å, K_b = 76(2) GPa (R^2 = 99.15 %), and c_0 = 6.7868(2) Å, K_c = 82(1) GPa (R^2 = 99.92 %).

As in the preceding subsection, we have fitted polynomials to the cell edge data (solid lines in Fig. 10a-c) and fitted 3rd order Birch-Murnaghan EoS to isotherms at 10 K intervals, again fixing the pressure derivatives at their *ab initio* values. We have also assumed that the relationship given in Eq. 4 can be said to be true for the unit cell edges and the axial incompressibilities; *e.g.*, for the *a*-axis,

$$a(T) = a_0 + b \ln (K_{a\,(0,0)} / K_{a\,(0,T)}) \quad (7)$$

For each of the three axes, we find that the incompressibilities can be divided into high- and low-temperature regimes, with a crossover between 100 – 160 K. Eq. 7 was fitted to the high- and low-temperature regimes of each axis; the resulting fits, and fit parameters, are shown in Fig. 14a-c.

As a matter of internal self consistency, the axial incompressibilites were used to calculated the bulk modulus from

$$K^{-1} = K_a^{-1} + K_b^{-1} + K_c^{-1} \quad (8)$$

Figure 14d shows how well the results of Eq. 8 agree with the results of fitting Eq. 4 to the volumetric data (solid line).

Table 3. Smoothed thermoelastic data for epsomite as a function of pressure and temperature.

T (K)	Unit cell volume (Å^3)	α_V $\times 10^4$ (K^{-1})	K_T (GPa)	δ_T
50	961.45	13.08	25.00	0.93
60	961.59	17.04	24.96	1.06
70	961.78	21.00	24.91	1.20
80	962.00	24.96	24.86	1.35
90	962.26	28.92	24.79	1.51
100	962.55	32.87	24.71	1.68
110	962.89	36.82	24.62	1.85
120	963.26	40.76	24.52	2.03
130	963.67	44.70	24.41	2.22
140	964.12	48.63	24.29	2.42
150	964.61	52.56	24.16	2.62
160	965.14	56.48	24.03	2.83
170	965.70	60.40	23.88	3.06
180	966.30	64.30	23.73	3.29
190	966.94	68.20	23.56	3.53
200	967.62	72.10	23.39	3.78
210	968.34	75.98	23.21	4.05
220	969.09	79.86	23.02	4.33
230	969.89	83.72	22.83	4.62
240	970.72	87.58	22.62	4.93
250	971.59	91.42	22.41	5.25
260	972.49	95.26	22.20	5.59
270	973.44	99.08	21.97	5.96
280	974.42	102.89	21.74	6.34
290	975.45	106.70	21.50	6.74
300	976.51	110.48	21.26	7.17

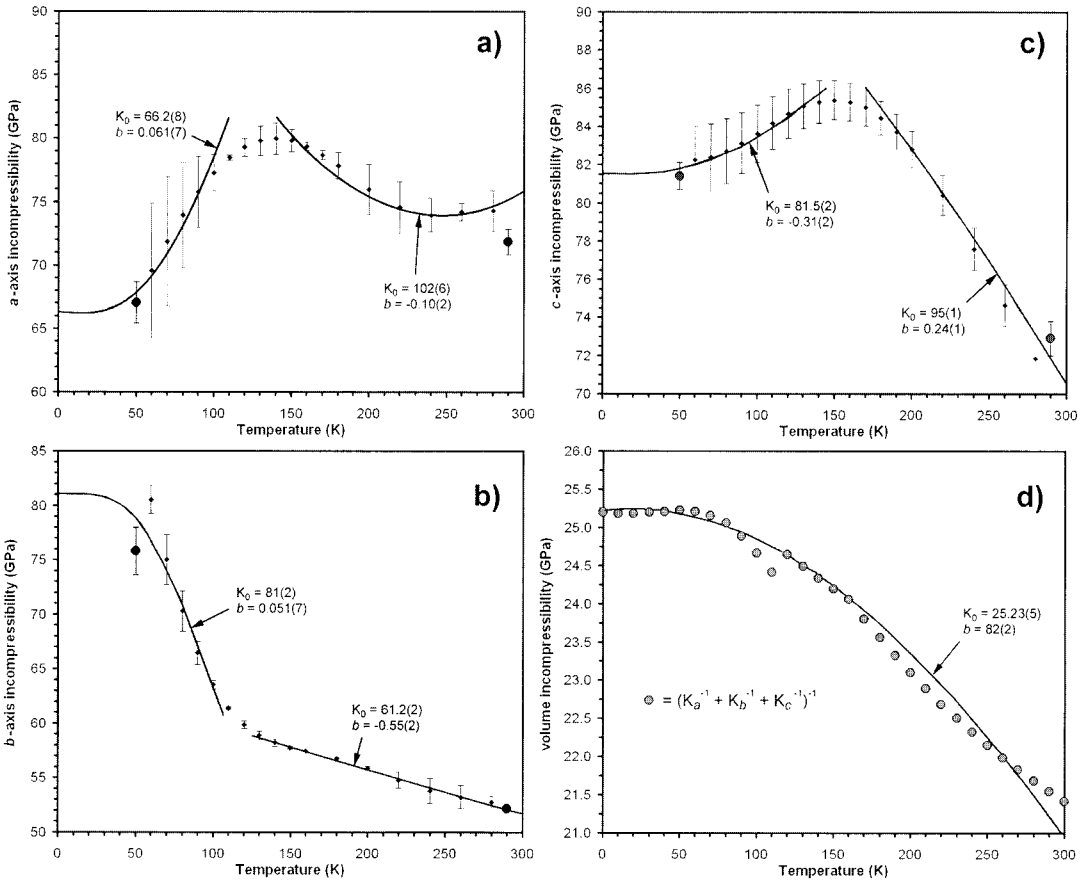

Fig. 14a-c. Model temperature dependence of the axial incompressibilities, K_a, K_b, and K_c. The two accurately determined isothermal moduli, from the 50 K and 290 K data, are shown with bold symbols; the lighter toned symbols are fits to just three points at each temperature (see text). Two-piece model fits are shown as bold lines, with fit coefficients indicated.

Fig. 14d. Model temperature dependence of the isothermal bulk modulus (K_T) determined from the model axial incompressibilities (filled circles) and compared with the model (solid line) found in Fig. 13.

Table 4. The measured elastic moduli of epsomite crystals as used for comparison with our experimental and computational results.

	Sundara Rao (1950)[1]		Voronkov (1958)[2]		Alexandrov *et al.* (1963)[3]	
ij	c_{ij}	s_{ij}	c_{ij}	s_{ij}	c_{ij}	s_{ij}
11	69.8	0.0245	40.3	0.0526(10)	32.5(7)	0.0516
22	52.9	0.0341	37.2	0.0622(1)	28.8(6)	0.0620
33	82.2	0.0150	35.1	0.0569(1)	31.5(6)	0.0567
12	39.0	-0.0166	26.7	-0.0268(1)	17.4(17)	-0.0194
13	28.2	-0.0027	23.6	-0.0170(2)	18.2(18)	-0.0186
23	28.3	-0.0061	24.1	-0.0247(1)	18.2(18)	-0.0246
44	10.7	0.0935	7.7	0.1300(5)	7.8(2)	0.1282
55	23.3	0.0429	16.1	0.0623(10)	15.6(3)	0.0641
66	22.2	0.0450	8.3	0.1207(2)	9.0(2)	0.1111

[1]Author tabulates c_{ij} and s_{ij} – no standard errors given.
[2]Author gives s_{ij}; used by us to calculate c_{ij}.
[3]Author gives c_{ij}; used by us to calculate s_{ij}. Errors are quoted as 2 –3 % on c_{ii} and 10 – 12 % on c_{ij}.

4. Discussion of results

In terms of the thermal expansion, there is little data in the literature with which to draw a comparison. Joule & Playfair (1849) measured the density of epsomite at ~ 0°C and ~ 32°C, deriving an average expansivity (at ~ 16°C) of 101.9×10^{-6} K^{-1}. This is in agreement with the value found here for deuterated epsomite at 16°C, $\approx 107 \times 10^{-6}$ K^{-1}.

The nine independent elastic moduli of epsomite were measured by Sundara Rao (1950), Voronkov (1958) and Alexandrov *et al.* (1963) at room pressure and temperature. The values from these studies disagree significantly (see Table 4). Following Ravindran *et al.* (1998), we have employed these measured elastic constants to calculate the bulk and linear incompressibilities of epsomite for comparison with Bridgman (1948a,b) and with our own findings (Table 2). The values in Table 2 column 4 (under Bridgman 1948b) were found by fitting a 3rd order Birch-Murnaghan EoS to his tabulated results, themselves smoothed and not the actual data. It is immediately clear that, of the three elastic modulus studies, only the results of Alexandrov *et al.* (1963) are in good agreement with the compression data of Bridgman and ourselves, and with our *ab initio* calculations. The moduli of Sundara Rao (1950) are too large by a factor of approximately two and the results of Voronkov (1958) are also in doubt.

The results of the *ab initio* calculations are in very good agreement with our experimental results. The calculated V_0 is larger than the experimental volume at 1.8 K by 3.8 %, which is comparable with results for other hydrogen-bonded crystals (*e.g.*, Fortes 2004). This ΔV corresponds to a dilation (or negative pressure) of 0.97 GPa. The calculated bulk modulus at the experimental V_0 is 28.3 GPa, which is ~ 10 % larger than the value found in Section 3.2.1.

The results of this work now allow us to calculate the density of an icy moon's salt hydrate mantle, given an assumed thermal profile, to a depth of roughly 500 km (corresponding to the likely depth at which a high-pressure polymorph of epsomite would become stable). This work, in combination with further measurements (and calculations) of the rheology and thermal conductivity of epsomite will make it possible to model thermal evolution and convection in the upper mantles of the large icy Jovian moons. The study presented here also provides a starting point for investigation of high-pressure epsomite polymorphs and studies of the volume change between epsomite and Fritzsche's salt (*e.g.*, Fortes *et al.*, 2004) as a function of pressure, the dehydration reaction having been implicated in global rifting on Jupiter's moon Ganymede (Day *et al.*, 2002; Hogenboom *et al.*, 2002).

5. Summary

We have used time-of-flight powder neutron diffraction to measure the molar volume of $MgSO_4.7D_2O$ (i) from 1.8 – 300 K at ambient pressure, (ii) from 50 – 290 K at 1.4, 3.0, and 4.5 kbar, (iii) from 0 – 5.5 kbar at 290 K, and (iv) from 0 – 4.5 kbar at 50 K. This has allowed us to determine the temperature dependence of the incompressibility, $(\partial K/\partial T)_P$, (thermodynamically equivalent to the pressure dependence of the thermal expansion, $(\partial\alpha/\partial P)_T$) of epsomite throughout its stability field. We observed that the *a*-axis exhibits negative thermal expansion from 30 – 250 K at room pressure, turning positive above 250 K and being zero below 30 K. However, each of the crystallographic axes exhibits a change in $(\partial\alpha/\partial T)$ at ~ 125 K, and this corresponds to significant changes in the axial incompressibilities; the *a*- and *c*-axes soften, and the *b*-axis stiffens considerably below ~ 125 K. Our thermoelastic results are in agreement with *ab initio* calculations at zero Kelvin, although the calculations offer no insight into the mechanism responsible for the change in behaviour at low temperatures. We observed no new polymorphs of epsomite, either at low temperatures or at high pressures, showing that the ambient-P,T structure remains stable to at least 5.5 kbar at 300 K without dehydrating or assuming a new crystal structure.

Acknowledgements: ADF acknowledges funding for this work from the Particle Physics and Astronomy Research Council (PPARC), U.K., grant number PPA/P/S/2003/00247: MA is funded by the Natural Environment Research Council (NERC), U.K., and LV is funded by a fellowship from the Royal Society. The authors are grateful to the ISIS facility for beam-time, and to John Dreyer, Andy Church, Chris Goodway and Jon Bones for technical support.

References

Alexandrov, K.S., Rhyzhova, T.V., Rostuntseva, A.I. (1963): Elastic properties of some sulfate heptahydrate crystals. *Sov. Phys. Crystallogr.*, **7**, 753-755.

Ashcroft, N.W. & Mermin, N.D. (1976): *Solid State Physics*. Harcourt Brace College Publishers, Orlando, Florida.

Barieau, E.E. & Giauque, W.F. (1950): $ZnSO_4.7H_2O$. $ZnSO_4.6H_2O$. Heat capacities, entropies and crystal perfection at low temper-

atures. Heats of solution and transition. *J. Am. Chem. Soc.*, **72**, 5676-5684.

Baur, W.H. (1964): On the crystal chemistry of salt hydrates. IV. The refinement of the crystal structure of $MgSO_4.7H_2O$ (Epsomite). *Acta Cryst.*, **17**, 1361-1369.

Birch, F. (1952): Elasticity and constitution of the Earth's interior. *J. Geophys. Res.*, **57**(2), 227-286.

Bridgman, P.W. (1948a): Rough compression of 177 substances to 40,000 kg/cm². *Proc. Am. Acad. Arts Sci.*, **76**, 71-87.

— (1948b): The linear compression of various single crystals to 30,000 kg/cm². *Proc. Am. Acad. Arts Sci.*, **76**, 89-99.

Brown, P.J. & Matthewman, J.C. (1993): Report RAL-93-009, Rutherford Appleton Laboratory, Oxfordshire.

Calleri, M., Gavetti, A., Ivaldi, G., Rubbo, M. (1984): Synthetic epsomite, $MgSO_4.7H_2O$: Absolute configuration and surface features of the complementary {111} forms. *Acta Cryst., Sect. B: Struct. Sci.*, **B40**, 218-222.

Cox, W.P., Hornung, E.W., Giauque, W.F. (1955): The spontaneous transformation from macrocrystalline to microcrystalline phases at low temperatures. The heat capacity of $MgSO_4.6H_2O$. *J. Am. Chem. Soc.*, **77**, 3935-3938.

Dalton, J.B., Prieto-Ballesteros, O., Kargel, J.S., Jamieson, C.S., Jolivet, J., Quinn, R. (2005): Spectral comparison of heavily hydrated salts with disrupted terrains on Europa. *Icarus*, **177**, 472-490.

Day, S., Asphaug, E., Bruesch, L. (2002): Cumulates, dykes and pressure solution in the ice-salt mantle of Europa. *EOS. Trans. Am. Geophys. Union*, **84**(46), Fall Meeting Suppl. P72B-0507.

Feldman, W.C., Mellon, M.T., Maurice, S., Prettyman, T.H., Carey, J.W., Vaniman, D.T., Fialips, C.I., Kargel, J.S., Elphic, R.C., Funsten, H.O., Laurence, D.J., Tokar, R.L. (2004): Contributions from hydrated states of $MgSO_4$ to the reservoir of hydrogen at equatorial latitudes on Mars. *Lunar Planet. Sci. Conf.*, **35**, #2035.

Ferraris., G., Jones, D.W., Yerkess, J. (1973): Refinement of the crystal structure of magnesium sulphate heptahydrate (Epsomite) by neutron diffraction. *J. Chem. Soc. Dalton Trans.*, **1973**, 816-821.

Fortes, A (2004): "Computational and experimental studies of solids in the ammonia-water system". Ph.D Thesis, University of London.

Fortes, A.D. (2005): From Surrey to the moons of Jupiter (via Mars): the story of Epsomite. *Axis*, **1**(9), 1-28. http://www.MineralogicalRecord.com

Fortes, A.D., Wood, I.G., Knight, K.S., Brodholt, J.P., Alfredsson, M., McGrady, G., Vočadlo, L. (2003): A high resolution neutron powder diffraction study of ammonia dihydrate ($ND_3.2D_2O$) phase I. *J. Chem. Phys.*, **119**, 10806-10813.

Fortes, A.D., Wood, I.G., Vočadlo, L., Alfredsson, M. (2004): ISIS Experimental Report RB 15133, Rutherford Appleton Laboratory, Oxfordshire.

Fortes, A.D., Wood, I.G., Alfredsson, M., Vočadlo, L., Knight, K.S. (2005): The thermal expansion and incompressibility of D_2O ice II from powder neutron diffraction. *J. Appl. Cryst.*, **38**, 612-618.

Finney, J. L. (1995): The complementary use of X-ray and neutron diffraction in the study of crystals. *Acta Cryst., Sect. B: Struct. Sci.*, **B51**, 447-467.

Frederiksson, K. & Kerridge, J.F. (1988): Carbonates and sulfates in CI chondrites – Formation by aqueous alteration on the parent body. *Meteorit.*, **23**, 35-44.

Fronczek, F.R., Collins, S.N., Chan, J.Y. (2001): Refinement of ferrous sulfate heptahydrate (melanterite) with low temperature CCD data. *Acta Cryst., Sect. E: Struct. Rep.*, **E57**, i26-i27.

Grasset, O., Sotin, C., Mousis, O., Mevel, L. (2001a): High pressure experiments in the system $MgSO_4$ – H_2O: Implications for Europa. *Lunar Planet. Sci. Conf.*, **31**, abstract 1386.

Grasset, O., Mevel, L., Mousis, O., Sotin, C. (2001b): The pressure dependence of the eutectic composition in the system $MgSO_4$ – H_2O: Implications for the deep liquid layer of icy satellites. *Lunar Planet. Sci. Conf.*, **31**, abstract 1524.

Grover, R., Getting, I.C., Kennedy, G.C. (1973): Simple compressibility relation for solids. *Phys. Rev. B*, **7**, 567-571.

Hardie, L.A. (1984): Evaporites - marine or non-marine ? *Amer. J. Sci.*, **284**(3), 193-240.

Hogenboom, D.L., Kargel, J.S., Ganasan, J.P., Lee, L. (1995): Magnesium sulfate-water to 400 MPa using a novel piezometer: densities, phase equilibria and planetological implications. *Icarus*, **115**, 258-277.

Hogenboom, D.L., Kargel, J.S., Daly, M.E. (2001): Stable and metastable high-pressure phases of the sulphuric acid – magnesium sulfate – water system: applications to Europa. *Lunar Planet. Sci. Conf.*, **31**, abstract 1739.

Hogenboom, D.L., Kargel, J.S., Reiter, M.L., Khor, Y.N. (2002): Volume changes attending hydration of quenched magnesium sulfate brine – the tectonics of Ganymede's sulci. *Lunar Planet. Sci. Conf.*, **33**, abstract 1638.

Hohenburg, P. & Kohn. W. (1964): Inhomogenous electron gas. *Phys. Rev.*, **136**, B864-B871.

Ibberson, R.M., David, W.I.F., Knight, K.S. (1992): "The High Resolution Neutron Powder Diffractometer (HRPD) at ISIS - A User Guide". RAL-92-031. Rutherford Appleton Laboratory, Oxfordshire, U.K.

Joule, J.P. & Playfair, L. (1849): Researches on atomic volume and specific gravity. 4. Expansion by heat of salts in the solid state. *Quart. J. Chem. Soc.*, **1**, 121-139.

Kargel, J.S. (1991): Brine volcanism and the interior structure of asteroids and icy satellites. *Icarus*, **94**, 368-390.

Kargel, J.S., Kaye, J.Z., Head, J.W., Marion, G.M., Sassen, R., Crowley, J. K., Prieto-Ballesteros, O., Grant, S.A., Hogenboom, D.L. (2000): Europa's crust and ocean: Origin, composition and the prospects for life. *Icarus*, **148**, 226-265.

Kohn, W. & Sham, L.J. (1965): Self-consistent equations including exchange and correlation effects. *Phys. Rev.*, **140**, A1133-A1138.

Kopp, H. (1865): Investigations of the heat capacity of solid bodies. *Phil. Trans. Roy. Soc. London*, **155**, 71-202.

Kresse, G. & Furthmüller, J. (1996): Efficient iterative schemes for *ab initio* total energy calculations using a plane wave basis set. *Phys. Rev. B*, **54**, 11169-11186.

Langlet, J., Bergès, J., Reinhardt, P. (2004): An interesting property of the Perdew-Wang 91 density functional. *Chem. Phys. Lett.*, **396**, 10-15.

Larsen, A.C. & Von Dreele, R.B. (1988): General Structure Analysis System (GSAS). Los Alamos National Laboratory Report LAUR B6-748, Los Alamos, New Mexico.

Lipiński, I.E., Kuriata, J. Natkaniec, I., Pawlokojć, A. (2001): Neutron scattering study of sodium ammonium sulfate dihydrate. *Phys. Stat. Solidi B*, **227**, 477-483.

Livshits, L.D., Genshaft, Yu. S., Ryabin, Yu. N. (1963): Equilibrium diagram of the crystal hydrates of $MgSO_4$ at high pressures. *Russ. J. Inorg. Chem.*, **8**, 676-678.

McCord, T.B., Hansen, G.B., Hibbitts, C.A. (2001): Hydrated salts on Ganymede's surface: evidence of an ocean below. *Science*, **292**, 1523-1525.

McKinnon, W.B. (2002): Sulfate content of Europa's ocean and shell: geological and astrobiological implications. *Am. Astr. Soc. DPS Meeting*, **34**, abstract 41.01.

McKinnon, W.B. & Zolensky, M.E. (2003): Sulfate content of Europa's ocean: Evolutionary considerations. *Am. Astr. Soc. DPS Meeting*, **35**, abstract 06.02.

Monkhorst, H.J. & Pack, J.D. (1976): Special points for Brillouin zone integrations. *Phys. Rev. B*, **13**, 5188-5192.

Nakamura, R.S. (2003): High pressure sulfate-water system in the large icy satellites. *Eos Trans. AGU*, **84**(46), Fall Meeting Suppl., Abstract P51B-0449.

Orlando, T.M., McCord, T.B., Grieves, G.A. (2005): The chemical nature of Europa's surface material and the relation to a subsurface ocean. *Icarus*, **177**, 528-533.

Pawley, G.S. (1981): Unit-cell refinement from powder diffraction scans. *J. Appl. Cryst.*, **14**, 357-361.

Perdew, J.P. (1991): *In* "Electronic Structure of Solids" (P. Zeische and H. Eschrig, Eds), Akademie, Berlin, p11.

Perdew, J.P. & Wang, Y. (1992): Accurate and simple analytic representation of the electron-gas correlation energy. *Phys. Rev. B*, **45**, 13244-13249.

Prieto, O. & Kargel, J.S. (2001): Specific heat capacity data of some hydrated salts at low temperatures. Applications to Europa satellite. *Lunar Planet. Sci. Conf.*, **32**, abstract 1625.

Ptasiewicz-Bak, H., Olovsson, I., McIntyre, G.J. (1997): Charge density in orthorhombic $NiSO_4.7H_2O$ at room temperature and 25 K. *Acta Cryst., Sect. B: Struct. Sci.*, **B53**, 325-336.

Raju, S., Sivasubramanian, K., Mohandas, E. (2002): The relation between bulk modulus and relative enthalpy: a broad-based thermodynamic analysis and a case study on aluminium. *Materials Lett.*, **54**, 13-20.

Ravindran, P., Fast, L., Korzhavyi, P.A., Johansson, B. (1998): Density functional theory calculations of elastic properties of orthorhombic crystals: Application to $TiSi_2$. *J. Appl. Phys.*, **84**, 4891-4904.

Spaun, N.A. & Head III, J.W. (2001): A model of Europa's crustal structure: recent Galileo results and implications for an ocean. *J. Geophys. Res.*, **106** (E4), 7567-7576.

Sundara Rao, R.V.G. (1950): Elastic constants of the heptahydrates of magnesium and zinc sulphate. *Proc. Indian Acad. Sci. A*, **31**, 365-370.

Tsuzuki, S. & Lüthi, H.P. (2001): Interaction energies of van der Waals and hydrogen bonded systems calculated using density functional theory: Assessing the PW91 model. *J. Chem. Phys.*, **114**, 3949-3957.

Vanderbilt, D. (1990): Soft self-consistent pseudopotentials in a generalized eigenvalue problem. *Phys. Rev. B*, **41**, 7892-7895.

Vočadlo, L., Knight, K.S., Price, G.D., Wood, I.G. (2002): Thermal expansion and crystal structure of FeSi between 4K and 1173K determined by time-of-flight neutron powder diffraction. *Phys. Chem. Minerals*, **29**, 132-139.

Voronkov, A.A. (1958): The piezoelectric, elastic and dielectric properties of crystals of $MgSO_4.7H_2O$. *Sov. Phys. –Crystallogr.*, **3**, 722-725

Wallace, D.C. (1998): "Thermodynamics of Crystals". Dover, New York.

Wood, I.G., Knight, K.S., Price, G.D., Stuart, J.A. (2002): Thermal expansion and atomic displacement parameters of cubic $KMgF_3$ perovskite determined by high resolution neutron powder diffraction. *J. Appl. Cryst.*, **35**, 291-295.

Zolotov, M. Yu., Kuzmin, R.O., Shock, E.L. (2004): Mineralogy, abundance, and hydration state of sulfates and chlorides at the Mars Pathfinder landing site. *Lunar Planet. Sci. Conf.*, **35**, #1465.

Received 15 July 2005
Modified version received 21 December 2005
Accepted 3 April 2006